

# Universal robust quantum gates by geometric correspondence

Yong-Ju Hai,<sup>1,2</sup> Junning Li,<sup>3,4</sup> Junkai Zeng,<sup>1,4</sup> Dapeng Yu,<sup>1,2,4</sup> and Xiu-Hao Deng<sup>1,4,\*</sup>

<sup>1</sup>*Shenzhen Institute for Quantum Science and Engineering (SIQSE),  
Southern University of Science and Technology, Shenzhen, P. R. China*

<sup>2</sup>*Department of Physics, Southern University of Science and Technology, Shenzhen 518055, China*

<sup>3</sup>*Department of Physics, City University of Hong Kong,  
Tat Chee Avenue, Kowloon, Hong Kong SAR, China*

<sup>4</sup>*International Quantum Academy (SIQA), and Shenzhen Branch,  
Hefei National Laboratory, Futian District, Shenzhen, P. R. China*

Precise and robust quantum control is the key to emerging quantum technologies. We uncover the essential correspondence between driven noisy quantum evolution and multiplex space curves, whose properties provide an explicit geometric characterization of the dynamics. Based on this, we develop the theory to tackle generic quantum errors and prove its necessary and sufficient conditions. Our analytic-numerical hybrid protocol enables the construction of universal robust quantum gates with very simple pulses for any given gate time. Our numerical tests demonstrate plateaus of gate fidelity above the fault-tolerance threshold over a broad range of noise strength, based on realistic models of semiconductor spin qubits and superconducting transmons. Our theory is ready to assist the leap of quantum information processing in various physical platforms.

## I. INTRODUCTION

The future promises of applicable quantum technologies are brought closer to the present-day reality along with the recent breakthroughs [1–4]. One of the key ingredients that triggers these advances is precise and robust quantum control [5–8], which is approaching the fault-tolerant threshold in isolated characterization of up-to-date quantum processors [9–12]. Nonetheless, controlling a realistic multi-qubit system remains challenging since the coupling to classical or quantum environments induces quantum decoherence and gate errors. Also, in contrast to feedback control with overhead on the hardware level, robust control is engineered in the feed-forward flavor to dynamically correct the errors [13, 14], and hence plays an important role in the integration of massive qubits [15–19]. Practical robust gates are commonly synthesized with pulse-shaping techniques leveraging numerical optimization [20–25], whose growing computational cost hinders the further applications. Therefore, fundamental solution to this issue relies on understanding the origin of robustness and the search of conserved quantities in noisy quantum evolution. Quantum geometry associated with the adiabatic passage has been found useful for robust control [26–30]. To speed up the control, dynamically correcting gates is proposed from geometric space curves [14, 31, 32] and reveals a promising solution for accurately controlling noisy qubits.

However, the application of the geometric theory for universal robust control needs to resolve the following fundamental issues: 1. The geometric essence of the noisy quantum dynamics remains to be seen, although a mapping between the control pulses and geometric space curves was found. Also, this mapping is not self-

consistent because the singularity arises at the vanishing-curvature points. Furthermore, the non-negative definition of curvature forces the pulses to be non-negative. An essential picture is needed to generalize to multiplex curves or higher dimensions. 2. There still needs to be a quantitative measure of control robustness, and a geometrically intuitive theory should give an exact quantity for the measure. 3. Universal robust quantum control should include universal gates for generic noises. Nevertheless, the previous studies have been limited to single-qubit gates and single errors. 4. Practical robust control requires the automatic generation of the pulses for given system parameters. But there has yet to be an algorithmic protocol exploiting the geometric theory. 5. The previous study was limited to a toy model, which needs to include more realistic issues. Applying the framework requires a more detailed study of both robust single-qubit and two-qubit gates in solving the impending control problems in realistic qubit systems.

In this manuscript, we study the essential correspondence of the noisy quantum dynamics to multiple geometric curves, which are parametrized in generalized Frenet-Serret frames. We develop a framework that enables the characterization of the error susceptibility of driven quantum dynamics subject to generic noises. The necessary and sufficient conditions in the framework guide the framework’s application to robust control. We also present a general and systematic protocol for searching arbitrary robust control pulses with the simplest waveforms, containing only a few Fourier components for any given gate time, which is compatible with experimental constraints. We perform numerical simulations to demonstrate the framework’s effectiveness based on the realistic multi-qubit models of semiconductor quantum dots and superconducting transmons. We obtain universal robust quantum gates that feature high-fidelity plateaus above the fault-tolerant threshold over a broad range of noise strength.

---

\* dengxh@sustech.edu.cn

## II. ANALYTICAL THEORY

### A. Model settings

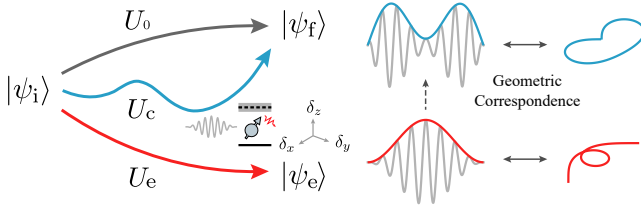


FIG. 1. The geometric correspondence of noisy quantum dynamics. The black trajectory corresponds to the ideal unitary evolution  $U_0$  that drives the initial quantum state to the desired final state. Realistic systems subject to errors in the longitudinal direction,  $\delta_z$ , and transverse direction,  $\delta_x$  and  $\delta_y$  undergo the colored trajectories with different control fields. The blue and red evolution trajectories are respectively driven by the robust pulse (blue) and cosine pulse (red) in the middle, corresponding to the blue and red geometric curves on the right.

We start from the generic Hamiltonian with a control field

$$H(t) = H_0 + H_c(t) + V. \quad (1)$$

Here the system Hamiltonian  $H_0$  added with the control term  $H_c(t)$  generates the desired time evolution.  $V = \boldsymbol{\delta} \cdot \hat{\mathbf{O}}$  is the noise term, where vector  $\boldsymbol{\delta}$ 's components are random complex numbers corresponding to quantum and classical noises [33, 34] that couple to the target quantum system via the operators  $\hat{\mathbf{O}} = \{O_1, \dots, O_n\}$ . In the  $SU(2)$  subspace,  $\hat{\mathbf{O}} = \hat{\boldsymbol{\sigma}}$  and  $\hat{\boldsymbol{\sigma}}$  is the vector of Pauli operators.  $\boldsymbol{\delta}$  is generally time-dependent and randomly fluctuating, which could be caused by unwanted effects including uncontrollable frequency shifts, spectrum broadening, crosstalk, parameter fluctuations, residual couplings [35, 36], etc.

The idea of robust control using the geometric correspondence is illustrated in Fig. 1. A trivial control field  $H_c(t)$ , for example, a cosine pulse, supposedly drives the raw system  $H_0$  to an target final state  $|\psi_f\rangle$ . But subject to the noise  $V$ , the system's evolution deviates from the ideal trajectory  $U_0$  and undergoes a noisy evolution  $U_e$ . The erroneous final state  $|\psi_e\rangle$  has an unknown distance from the desired final state depending on the noise strength. To correct the errors, control Hamiltonian  $H_c(t)$  formed with robust control pulse (RCP) obtained by geometric correspondence should drive the system to the expected state  $|\psi_f\rangle$ , disregarding the presence of the unknown errors. This means that at some time  $\tau$ ,  $U_c(\tau) = U_0$ . Nonetheless, solving the RCP is very challenging. We will show how to formulate error measure of control pulses and construct arbitrary RCPs, by establishing the geometric correspondence between space curves and the noisy quantum dynamics.

In order to obtain analytical solutions, our theory is formulated on the two-state systems, giving the  $SU(2)$  dynamics. The dynamics of higher dimensional systems correspond to more complex geometric structures and is beyond the scope of this manuscript. However, some complex system's dynamics could be decomposed into direct sums or products of  $SU(2)$  operators, then the work presented in this manuscript still apply. The raw Hamiltonian for a single two-state Hilbert space  $\text{span}\{|a\rangle, |b\rangle\}$  is  $H_{\text{raw}} = -\frac{\omega}{2}\sigma_z$ . If driven transversely with a control field, it is usually written in the rotating frame with the control field

$$H_0^{\text{rot}} = -\frac{\Delta}{2}\sigma_z, \quad (2)$$

where  $\Delta$  is the detuning between qubit frequency and control field. The formulas in this manuscript are all present in the rotating frame, so in the following we will drop the superscript "rot". The control and the noise Hamiltonian could be written in the general form

$$H_c(t) = \Omega_z(t)\sigma_z + \Omega_x(t)\sigma_x + \Omega_y(t)\sigma_y \quad (3)$$

$$V = \delta_z\sigma_z + \delta_x\sigma_x + \delta_y\sigma_y, \quad (4)$$

where the Pauli matrices  $\sigma_x = |a\rangle\langle b| + |b\rangle\langle a|$ ,  $\sigma_y = -i|a\rangle\langle b| + i|b\rangle\langle a|$ ,  $\sigma_z = |a\rangle\langle a| - |b\rangle\langle b|$ .

The error  $\delta_z$  is related to many types of longitudinal noises including variations in frequency or fluctuating spectral splitting, which could originate from the coupling to other quantum systems, e.g., the neighboring qubits, two-level defects, or quantum bath [37, 38]. On the other hand, the transverse errors  $\delta_x$  and  $\delta_y$  result from energy exchange with the environment, such as relaxation, crosstalk, and imperfect control. In this manuscript, the formulation of the theory assumes that the noise fluctuation time scale is longer than a quantum gate. So  $\boldsymbol{\delta}$  is a constant vector in this quasi-static limit.

Based on this assumption, we will show how to engineer the control Hamiltonian to correct the errors in its perpendicular directions. And hence for generic errors in the  $x, y, z$  directions we need controls in at least two directions, i.e., two terms out of the three in the control Hamiltonian in Eq. (3) are sufficient to achieve dynamical error suppression. Specifically in the following discussion, we let

$$H_c(t) = \frac{\Omega(t) \cos \Phi(t)}{2} \sigma_x + \frac{\Omega(t) \sin \Phi(t)}{2} \sigma_y, \quad (5)$$

where  $\Omega(t)$  and  $\Phi(t)$  are the control amplitude and modulated phase of the transverse control field.

### B. Geometric correspondence

Here we present the essential geometric correspondence between the quantum dynamics and space curves, based on which we further establish the robust control constraints. Given that the total time evolution reads

$U(t) = \mathcal{T} \exp\{-i \int_0^t H(\tau) d\tau\}$ , generated by the full noisy Hamiltonian  $H(t)$  given in Eq. (1), whereas the noiseless driven dynamics evolves as  $U_0(t) = \mathcal{T} \exp\{-i \int_0^t (H_0 + H_c(\tau)) d\tau\}$ . In the interaction picture with  $U_0(t)$ , the total Hamiltonian is transformed to  $V_I = U_0^\dagger V U_0 = U_0^\dagger (\boldsymbol{\delta} \cdot \hat{\boldsymbol{\sigma}}) U_0$ . Our model settings have assumed time-independent error, so  $\boldsymbol{\delta}$  is a constant for time-integral. For the  $j$ -component of the noise source, the transformation  $U_0^\dagger(t) \sigma_j U_0(t)$  over duration  $dt$  gives rise to a displacement of the operator  $d\mathbf{r}^j(t) \cdot \hat{\boldsymbol{\sigma}}$ , while its time derivative defines a velocity  $\mathbf{T}_j(t) = \dot{\mathbf{r}}^j(t)$ . As  $\|\mathbf{T}_j\| = \|U_0^\dagger(t) \sigma_j U_0(t)\| = 1$ ,  $\mathbf{T}_j$  is a unit vector which means the  $j$ -error motion has a constant speed. So the Hamiltonian has the geometric correspondence

$$\begin{aligned} V_I(t) &= \delta_x \mathbf{T}_x(t) \cdot \hat{\boldsymbol{\sigma}} + \delta_y \mathbf{T}_y(t) \cdot \hat{\boldsymbol{\sigma}} + \delta_z \mathbf{T}_z(t) \cdot \hat{\boldsymbol{\sigma}} \\ &= \sum_{j,k=x,y,z} \delta_j T_{jk}(t) \sigma_k. \end{aligned} \quad (6)$$

Here  $T_{jk}(t)$  is a tensor connecting  $j$ -component of the noise source  $\delta_j$  and Pauli term  $\sigma_k$ .

Because  $U(t) = U_0(t) U_I(t)$ ,  $U_I(t)$  could be called the *erroneous evolution* referring to the deviation of the noisy  $U(t)$  from the noiseless  $U_0(t)$ .  $U_I(t)$  is generated by the Hamiltonian in the interaction picture following the integral in time order as

$$\begin{aligned} U_I(t) &= \mathcal{T} \exp\{-i \int_0^t d\tau V_I(\tau)\} \\ &= \mathcal{T} \exp\{-i \sum_{j=x,y,z} \delta_j \int_0^t d\tau [\mathbf{T}_j(\tau) \cdot \hat{\boldsymbol{\sigma}}]\} \\ &= \mathcal{T} \exp\{-i \sum_{j=x,y,z} \delta_j \mathbf{r}^j(t) \cdot \hat{\boldsymbol{\sigma}}\}. \end{aligned} \quad (7)$$

Therefore, the erroneous dynamics generated by the Hamiltonian could be described by the kinematics of a moving point. The displacement  $\mathbf{r}^j(t)$  sketches a space curve in  $\mathbb{R}^3$ , corresponding to the error coupled to  $\sigma_j$ . So we call  $\mathbf{r}^j(t)$  the  *$j$ -error curve*. Therefore, the erroneous evolution  $U_I(t)$  could be described by three error curves. It is known that any continuous, differentiable space curve could be defined necessarily and efficiently with the Frenet-Serret frame [39, 40] with tangent, normal, and binormal unit vectors  $\{\mathbf{T}, \mathbf{N}, \mathbf{B}\}$ . Moreover, there is a correspondence between the curve length and the evolution time  $L(t) = \int_0^t d\tau \|\mathbf{T}_j(\tau) \cdot \hat{\boldsymbol{\sigma}}\| = \int_0^t d\tau = t$ . Using the  $j$ -error curve and its tangent vector defined above, the explicit geometric correspondence could be established.

As an example, for the control Hamiltonian Eq. (5) and noise in  $z$ -direction,  $H = \delta_z \sigma_z + H_c(t)$ . Following the derivation in Appendix A, the explicit geometric correspondence between the control Hamiltonian and the error curve is given by

$$\begin{aligned} \mathbf{T} \cdot \hat{\boldsymbol{\sigma}} &= U_0^\dagger(t) \sigma_z U_0(t) \\ \mathbf{N} \cdot \hat{\boldsymbol{\sigma}} &= U_0^\dagger(t) (-\sin \Phi(t) \sigma_x + \cos \Phi(t) \sigma_y) U_0(t) \\ \mathbf{B} \cdot \hat{\boldsymbol{\sigma}} &= U_0^\dagger(t) (-\cos \Phi(t) \sigma_x - \sin \Phi(t) \sigma_y) U_0(t). \end{aligned} \quad (8)$$

Combining Eq. (5) and Eq. (8) we get the relation between the Frenet vectors and the control Hamiltonian

$$\begin{cases} \kappa(t) = \dot{\mathbf{T}} \cdot \mathbf{N} = \Omega(t) \\ \tau(t) = -\dot{\mathbf{B}} \cdot \mathbf{N} = \dot{\Phi}(t), \end{cases} \quad (9)$$

where  $\kappa(t)$  and  $\tau(t)$  are respectively the signed curvature and the singularity-free torsion of  $z$ -error curve.

So far, we have established the geometric correspondence between the control Hamiltonian and the kinematic properties of space curves. This correspondence is a bijective map which means given either a Hamiltonian or a curve, its counterpart could be solved straightforwardly via Eq. (8) or Eq. (9). We refer to Appendix A and C for more details.

### C. Robust control

The robust control of the two-state system's dynamics requires the error evolution to vanish while driving the system to achieve a target gate at a specific gate time  $\tau$ , i.e., satisfying the robust condition  $U(\tau) = U_0(\tau)$  and  $U_I(\tau) = I$ . To obtain the explicit form of  $U_I$  in terms of the error curve, we use the equivalency between the time ordering representation and the Magnus expansion [41] to obtain

$$\begin{aligned} U_I(t) &= \exp\{-i \sum_n [(\delta \cdot)^n \hat{\mathbf{A}}_n(t)]\} \\ &= \exp\{-i[\delta_j A_1^j + \delta_j \delta_k A_2^{jk} + O(\delta^3)]\}, \end{aligned} \quad (10)$$

where  $\hat{\mathbf{A}}_n$  is  $n$ th-order tensor corresponding to  $n$ th-order of the Magnus series and the Einstein summation is used. We have also assumed that all the  $\delta_{x,y,z}$  terms are at the same perturbative order. The exponential form can also be further expanded to polynomial series

$$U_I(t) = I - i\delta_j A_1^j - \frac{1}{2}(\delta_j A_1^j)^2 + i\delta_j \delta_k A_2^{jk} + O(\delta^3), \quad (11)$$

where

$$\begin{cases} A_1^j(t) = \int_0^\tau du (\mathbf{T}_j \cdot \hat{\boldsymbol{\sigma}}) \\ A_2^{jk}(t) = \frac{1}{2} \int_0^\tau d\tau [\dot{A}_1^j(t), A_1^k(t)] \\ A_{n+1}^{jkl\dots}(t) = \frac{1}{2} \int_0^\tau d\tau [\dot{A}_n^j(t), A_n^{kl\dots}(t)]. \end{cases} \quad (12)$$

Utilizing the geometric correspondence present above, the robust constraints could be established up to arbitrary perturbative orders. Correcting the leading-order error at time  $\tau$  requires the first-order term  $A_1^j(t)$  in Eq. (11) to vanish. Using  $\mathbf{T}_j(t) = \dot{\mathbf{r}}^j(t)$  we get an explicit geometric representation of the erroneous evolution

$$A_1^j(t) = \mathbf{r}^j(t) \cdot \hat{\boldsymbol{\sigma}}. \quad (13)$$

The geometric correspondence of  $A_1^j(t)$  is given by the displacement  $\mathbf{r}^j(t)$  of the  $j$ -error curve. Therefore, the condition of control robustness up the leading order is

$$\mathbf{r}^j(\tau) = 0. \quad (14)$$

Eq. (12) infers that the higher order terms contains more complex geometric properties. For simplicity, we consider the case when the error lies in only one axis  $j$ . The second order term in Eq. (11)

$$A_2^{jj}(t) = i \int_0^t \dot{\mathbf{r}}^j(\tau) \times \mathbf{r}^j(\tau) d\tau \cdot \hat{\sigma} = i \mathbf{R}^j(t) \cdot \hat{\sigma}, \quad (15)$$

now has a geometric meaning that  $\mathbf{R}^j(t) = \int_0^t \dot{\mathbf{r}}^j(\tau) \times \mathbf{r}^j(\tau) d\tau$  forms directional integral areas on  $y$ - $z$ ,  $z$ - $x$ , and  $x$ - $y$  planes enclosed by the projections of the space curve. Similarly, the second-order robustness conditions requires  $\frac{1}{2}(\delta_j A_1^j)^2 + i\delta_j^2 A_2^{jj} = 0$ , i.e.,

$$\begin{cases} \mathbf{r}^j(\tau) = 0 \\ \mathbf{R}^j(\tau) = 0. \end{cases} \quad (16)$$

Higher-robustness conditions also refer to the vanishing net areas of the corresponding space curves only with more closed loops [32]. Nonetheless, higher order robustness means more constraints so that the search for control pulses becomes more challenging, and the resulting control pulses are typically longer and more complicated, making experimental realization infeasible. Therefore aiming at robustness for orders higher than two is usually unnecessary. We consider only the constraints up to leading terms in the pulses construction protocol presented in the following Section III.

To explain the assumption addressed at Eq. (5), we now present theorems to answer the questions: 1. What are the necessary conditions to correct the errors? 2. What are the sufficient conditions to correct the errors?

**Theorem:** (*Non-correctable condition*) If  $[V, H_c(t)] = 0$  for  $\forall t \in [0, \tau_g]$ , the erroneous evolution cannot be dynamically corrected. Specifically, if  $[\sigma_j, H_c(t)] = 0$ , the  $j$ -error cannot be dynamically corrected by  $H_c$ .

**Proof.** Using the geometric correspondence, the proof for this theorem becomes explicit and intuitive. A necessary condition for the dynamical correctability is that the velocity  $\mathbf{T}$  of the erroneous evolution could be modified by the control Hamiltonian, namely  $\mathbf{N} \neq 0$  at some time  $t \in [0, \tau_g]$ . Whether a trajectory  $\mathbf{r}$  is curved or not depends on its normal vector  $\mathbf{N}$ , corresponding to the dependence of erroneous evolution on  $H_c(t)$ . From the geometric correspondence introduced above, we know

$$\begin{aligned} \mathbf{N}(t) \cdot \hat{\sigma} &= \frac{d(U_0^\dagger V U_0)}{dt} \\ &= \dot{U}_0^\dagger V U_0 + U_0^\dagger \dot{V} U_0 + U_0^\dagger V \dot{U}_0 \\ &= U_0^\dagger [H_c, V] U_0. \end{aligned} \quad (17)$$

Here for quasi-static noise,  $\dot{V} = 0$  within the gate time. Therefore, if  $[V, H_c(t)] = 0$  for  $\forall t \in [0, \tau_g]$ ,  $\mathbf{N}(t) \equiv 0$ . In the geometric frame, it means that the error curve remains in the same direction and hence the erroneous evolution cannot be dynamically corrected.

Specifically, for  $j$ -error,  $V_j = \delta_j \sigma_j$ . The non-correctable condition  $[V, H_c] = 0$  becomes  $[\sigma_j, H_c] = 0$ . Q.E.D.

Following the general theorem, the following statement discusses the specific form of robust control Hamiltonian.

**Corollary:** (*Necessary condition*) Controls in two non-commutable directions are necessary to correct the quasi-static noises coupled to all  $x, y, z$  directions. That is  $H_c(t) = \Omega_j(t)\sigma_j + \Omega_k(t)\sigma_k$ , where  $[\sigma_j, \sigma_k] = i2\epsilon_{jkl}\sigma_l$ .

For any given  $j$ -error,  $H_c$  should contains at least one term that is non-commutable with  $\sigma_j$ . Eq. (5) gives an example where  $j = x, k = y$ . So it is easy to demonstrate that for general  $V = \delta \cdot \hat{\sigma}$ , we get  $[V, \Omega_j(t)\sigma_j + \Omega_k(t)\sigma_k] = i\gamma \cdot \hat{\sigma}$ , where vector  $\gamma(t) \neq 0$  for  $t \in [0, \tau_g]$ .

So far, we have answered the first question: the necessary conditions for the robust control. This helps clarify in which scenarios an error cannot be corrected dynamically. But whether it is feasible to perform robust control to correct arbitrary noisy quantum evolution remains unknown. Furthermore, whether there exist smooth and simple pulses for the robust control remains a question. To answer this, we address a conjecture here. We will next present analytical and numerical solutions to the universal robust gates, which correct errors subject to noises from all directions. These results are the proof to this conjecture.

**Conjecture:** (*Sufficient condition*) Controls in two directions are sufficient to correct the quasi-static noises coupled to all  $x, y, z$  directions. That is  $H_c(t) = \Omega_j(t)\sigma_j + \Omega_k(t)\sigma_k$ , where  $[\sigma_j, \sigma_k] = 2i\epsilon_{jkl}\sigma_l$ .

### III. CONSTRUCTING ROBUST CONTROL HAMILTONIAN

In this section, we will show how to utilize the geometric correspondence of quantum evolution to quantify the robustness of arbitrary quantum control pulse and further present a protocol to construct the universal robust control Hamiltonian for arbitrary noises.

#### A. Robustness measure

The error curves, being the geometric correspondence of the erroneous quantum dynamics, provide an intuitive measure of the robustness of control pulses. Specifically, let's define the *error distance* to be the first-order error  $\|\mathbf{r}^j(\tau)\|$ , as in Eq. (13). Unlike gate fidelity, the error distance describes the variation of gate fidelity subject to a specific noise. Therefore, quantitative characterization of the robustness for arbitrary gate implementations could be done by mapping the pulses to the error curves and then measuring the error distance. Fig. 2 shows the  $z$  error curves of a robust pulse and the two commonly used pulses in experiments, the cosine and sine pulses. Note that the coordinates of the planar error curves in the manuscript are all denoted by  $\{x, y\}$  for convenience. We numerically simulate the driven dynamics subject to error  $\delta_z \sigma_z$  and obtain the gate fidelity of the three pulses as shown in Fig. 2(c) to compare their robustness. The

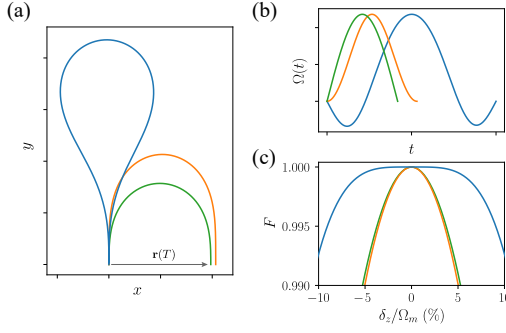


FIG. 2. (a) Error curves of RCP (blue), cosine (orange) and sine (green) pulses, corresponding to the pulse waveforms shown in (b). (c) Comparison of the fidelities versus the error strength for different pulse waveforms, as a demonstration of the agreement between the robustness behaviors of different pulses and their error distances.

fidelity of sine and cosine pulses cannot maintain a fidelity plateau as the RCP does, which agrees with their error distances illustrated in Fig. 2(a). Therefore, we will use the error distance as constraints in the following numerical pulse construction protocol. More quantitative analysis of the robustness order for various pulses could be found in Appendix B. This approach for quantifying noise susceptibility can be generalized to quantum systems with multiple error sources and multiple error curves. The simultaneous robustness to all the error sources requires the vanishing of error distances for all the curves. The examples of this case will be present in Section III C. Furthermore, the second-order error  $\|\mathbf{R}^J(\tau)\|$ , as introduced by Eq. (15), indicates an additional measure of the higher order control robustness and will be illustrated in Section III C and Appendix D.

## B. Pulse construction protocol

The geometric correspondence helps understand how the noise affects the qubit dynamics. Therefore, it provides a way to find the conditions of robust evolution and motivates a pulse construction protocol by reverse engineering analytic space curves that satisfy the robustness conditions. The procedure of this construction is summarized as follows: (1) Construct a regular curve that meets certain boundary conditions determined by the target gate operation and robustness conditions such as closeness and vanishing net area; (2) Re-parameterize the curve in terms of the arc-length parameter to make it moving at unit-speed; (3) Scale the length of the curve to fit an optional gate time; (4) Calculate its curvature and torsion to obtain the corresponding robust control pulses. This protocol are illustrated explicitly in previous works, where plane and space curves were used to construct different RCPs [14, 31, 32]. We note that in our generic geometric correspondence, the control pulses are related to signed curvature and singularity-free tor-

sion of the geometric curve, which are obtained by a set of well-chosen continuous Frenet vectors. We demonstrate the pulse construction from space curves and provide a universal plane curve construction for first- and second-order robust pulses in Appendix C and D.

However, even with the constraints given by the theory, it is still challenging to make a good guess of ansatz for the RCPs. In a real quantum computer, the universal gates using RCPs are desired to be generated automatically given the system parameters. Therefore, assistance with numerical search is needed to find the RCPs automatically using the robustness conditions.

Here, we present an analytic-numerical protocol to construct universal error-robust quantum gates that are made automatic. The theory of geometric correspondence gives analytical constraints for the robustness, which is added to the objective function to perform constrained optimization using the COCOA algorithm [25]. The protocol is described as follows.

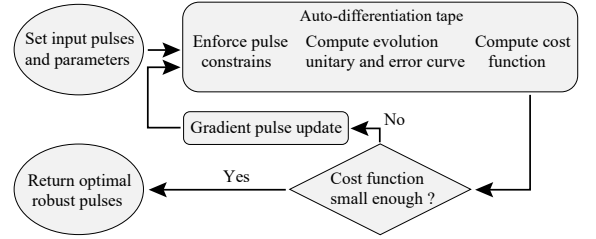


FIG. 3. The flow chart of the pulse construction protocol.

(1) Initialize. Set initial input pulses and other relevant parameters.

(2) Analytic pulse constraints. We apply discrete Fourier series as the generic ansatz of the RCPs, so that we can control the smoothness of the pulses by truncating the Fourier basis while limiting the number of parameters. For pulse amplitude, the Fourier series is multiplied with a sine function to ensure zero boundaries values, i.e., zero starting and ending of the pulse waveform. The ansatz of the pulse amplitude and phase takes the form

$$\begin{aligned}\Omega_0(a_j, \phi_j; t) &= \sin\left(\frac{\pi t}{T}\right) \left(a_0 + \sum_{j=1}^n a_j \cos\left(\frac{2\pi j}{T}t + \phi_j\right)\right) \\ \Phi_0(b_j, \psi_j; t) &= b_0 + \sum_{j=1}^n b_j \left(\frac{2\pi j}{T}t + \psi_j\right),\end{aligned}\tag{18}$$

where  $n$  is the number of Fourier components, which will be set to be of  $[1, 4]$  for different gates shown in this paper.  $\{a_j, \phi_j, b_j, \psi_j\}$ 's are parameters to be optimized. For each input pulse, the corresponding Fourier series is obtained by a Fourier expansion and truncation, and then the expansion function for the amplitude is multiplied with the sine function to obtain a modified pulse.

(3) Use the modified pulses to compute the dynamics to obtain the evolution operator  $U(t)$ , as well as the error curve  $\mathbf{r}(t)$ .

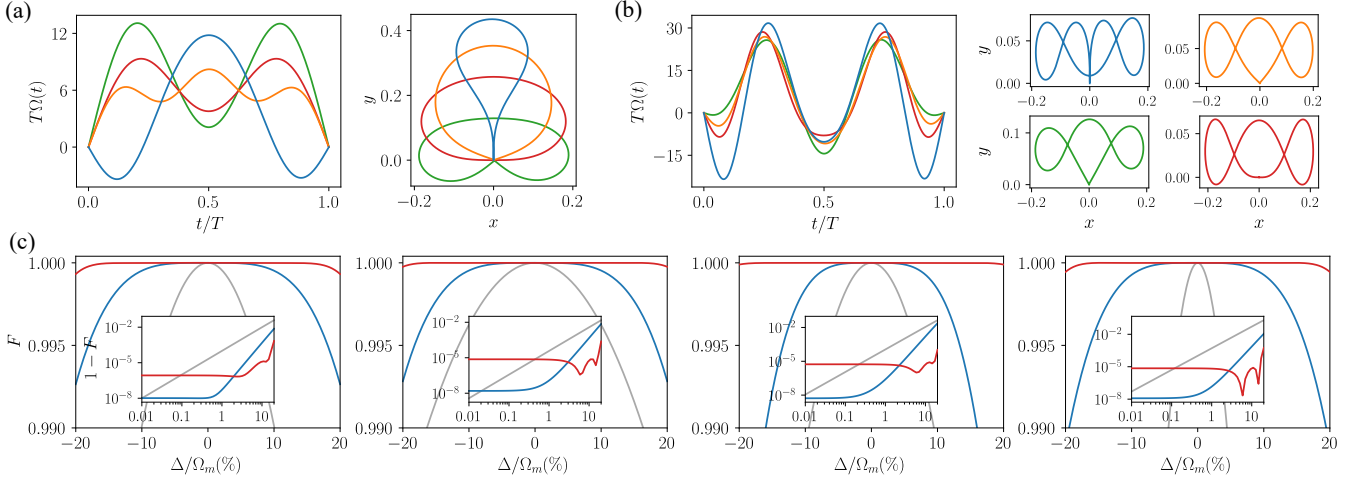


FIG. 4. (a) First order robust control pulses  $\{R_{1;\perp}^\pi, R_{1;\perp}^{7\pi/4}, R_{1;\perp}^{5\pi/2}, R_{1;\perp}^{2\pi}\}$  (blue, orange, green, red) and their corresponding error curves. (b) Extended-robust control pulses  $\{R_{\text{ex};\perp}^\pi, R_{\text{ex};\perp}^{9\pi/4}, R_{\text{ex};\perp}^{5\pi/2}, R_{\text{ex};\perp}^{2\pi}\}$  (blue, orange, green, red) and their corresponding error curves. (c) Fidelities of the four single-qubit gates  $\{X_\pi, X_{\pi/4}, X_{\pi/2}, X_{2\pi}\}$  (left to right) realized by the first-order RCPs (blue) as in (a), extended RCPs (red) as in (b), and their cosine pulse counterpart (grey) against detuning noise. Insets are the infidelity versus the relative noise strength for each gate in log-log scale.

(4) Compute the cost function, which takes the form

$$C = (1 - F) + \xi, \quad (19)$$

where  $F$  is the gate fidelity [42] and  $\xi$  is the robustness constraint. When only the first order robustness is considered,  $\xi = \|r(\tau)\|$ . Here  $\|r(\tau)\|$  is the error distance as defined in III A. The robustness against errors in different axes can be achieved by including the error distances of different error curves in the cost function. The auto-differentiation tape records the calculations in (2)-(4).

(5) Make a gradient update of the pulse to minimize  $C$ .

(6) Go back to step (2) with the updated pulse as input if the cost function is larger than a criterion  $\tau$ , such as  $10^{-5}$ .

(7) If  $C < \tau$ , break the optimization cycle and obtain the optimal robust pulse, which takes the analytical form of Eq. (18).

### C. Universal set of RCP

Using the pulse construction protocol introduced in the former subsection, we are able to generate RCPs that satisfy the robustness condition provided by the geometric correspondence. As a specific example, we now apply the protocol to search for a set of RCPs that implement X-axis rotation that is robust against detuning error. Then Eq. (1) now turns into

$$H = \frac{1}{2}\Omega(t)\sigma_x + \frac{1}{2}\Delta\sigma_z. \quad (20)$$

We first optimize the control pulses with the first order robustness around  $\Delta = 0$ . The obtained op-

timal RCPs are shown in Fig. 4(a) and denoted as  $\{R_{1;\perp}^\pi, R_{1;\perp}^{7\pi/4}, R_{1;\perp}^{5\pi/2}, R_{1;\perp}^{2\pi}\}$ . Here  $R_{1;\perp}^\theta$  represents the first order RCP for a rotation of angle  $\theta$  that is capable of correcting errors in its perpendicular directions and we denote the maximum absolute pulse amplitude as  $\Omega_m = \max\{|\Omega|\}$ .

Searching for higher-order robust pulses requires adding more terms associated with the higher-order robustness constraints, e.g., the net-area of the error curve, to the constraint term  $\xi$  in the cost function Eq. (19). However, we found that simply adding these constraints hinders the convergence of the algorithm at an unacceptable rate because the computation of these net areas involves complicated integrals over the error curve. We settle this issue by adding new terms to the cost function  $C$  with the gate fidelity and error distance at a non-vanishing  $\Delta$ . Specifically, we use  $C = \sum_{j=1,2}(F(\Delta_j) + \|r(\Delta_j, \tau)\|)$ , where  $\Delta_1 = 0$  and  $\Delta_2$  is chosen to be  $\pi/\tau$  according to the experimentalist's expectation. This ensures the resulting RCPs maintain high gate fidelities over a broader range of noise amplitude and thus lead to extended robustness. We then obtained a class of extended RCPs denoted as  $\{R_{\text{ex};\perp}^\pi, R_{\text{ex};\perp}^{9\pi/4}, R_{\text{ex};\perp}^{5\pi/2}, R_{\text{ex};\perp}^{2\pi}\}$  that are made by three cosine functions, and the error curve of them have net-areas close to zero, as shown in Fig. 4(b). The robustness of the eight RCPs mentioned above is further confirmed by calculating the first few Magnus expansion terms, as shown in Appendix B.

We use the first-order RCPs and the extended RCPs to implement four single-qubit robust gates  $\{X_\pi, X_{\pi/4}, X_{\pi/2}, X_{2\pi}\}$  ( $X_\theta$  represents a rotation of angle  $\theta$  around x-axis of the Bloch sphere). The first three gates together with robust  $Y_{\pi/2}$  gate, a.k.a. applying



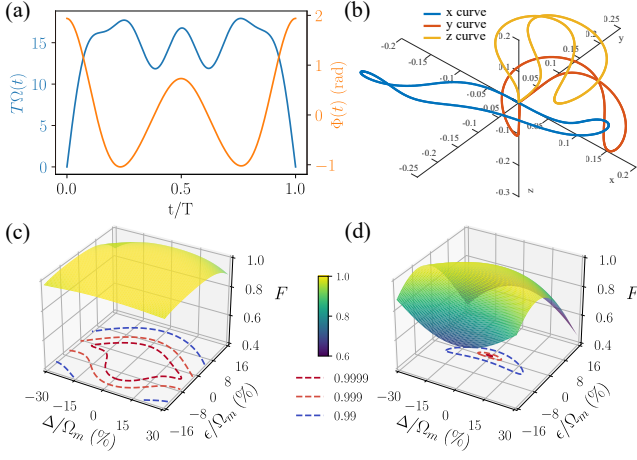


FIG. 5. (a) A set of RCPs  $R_{1;\text{all}}^{3\pi/2}\{\Omega(t), \Phi(t)\}$  are used to implement robust gate  $X_{3\pi/2}$  to correct all errors in x, y, z directions, with the closed x, y, z error curves (blue, orange, yellow) shown in (b). A comparison of gate fidelity against longitudinal and transverse error  $\delta$  and  $\epsilon$  using this  $R_{1;\text{all}}^{3\pi/2}$  and cosine pulse are shown in (c) and (d).

$R_{1;\perp}^{5\pi/2}$  or  $R_{\text{ex};\perp}^{5\pi/2}$  in the Y direction, are elementary single-qubit gates for a universal robust gate set [43], while the  $2\pi$  gate is equivalent to the robust dynamical decoupling. We numerically simulate the dynamics of the noisy qubit driven transversely (Eq. 20) and present the gate robustness in Fig. 4(c). Compared with the gates performed by trivial cosine pulses with the same maximal amplitudes of the RCPs, the gates using the first-order RCPs and extended RCPs all exhibit wide high-fidelity plateaus over a significant range of noise amplitude. The gate infidelities exhibit plateaus around  $10^{-8}$  within 1% noise region for first-order RCPs and  $10^{-5}$  within 15% noise region for extended RCPs. Note that high-fidelity plateaus are a sign of the robustness of the gates.

More general noises on all axes can be corrected simultaneously with XY control with the Hamiltonian in Eq. (5). This works because the robust control in a direction could correct the noise coupled to the other two perpendicular directions, as discussed in the previous section. As an numerical demonstration, we consider both longitudinal and transverse errors in the form of  $V = \frac{\Delta}{2}\sigma_z + \frac{\epsilon}{2}(\sigma_x + \sigma_y)$ , giving rise to the co-existence of x, y and z error curves in the geometric space. Then the robustness constraint in Eq. (19) takes the form  $\xi = \sum_{j=x,y,z} \|\mathbf{r}^j(\tau)\|$ . We apply our protocol to find a RCP  $R_{1;\text{all}}^{3\pi/2}$  with only four Fourier components to implement a single-qubit  $X_{3\pi/2}$  gate that is robust against errors in all three directions. Although this RCP is solved to generate a robust  $3\pi/2$  rotation around x-axis, its rotation axis can be changed by adding a constant phase while keeping the robustness along the rotation axis and its two perpendicular axes, as demonstrated numerically in Appendix B. As shown in Fig. 5(a) the XY drive has

three closed error curves during the gate time. The fidelity landscape of the  $X_{3\pi/2}$  gate using the  $R_{1;\text{all}}^{3\pi/2}$  and the cosine pulse in the two error dimensions is plotted in Fig. 5(b). The RCP shows a great advantage over the cosine pulse, showing a significant high-fidelity plateau with fidelity above 0.9999.

#### IV. UNIVERSAL ROBUST QUANTUM GATES FOR REALISTIC QUBITS

Applying this method to construct universal robust quantum gates for realistic systems, especially in a multi-qubit setup, is not a trivial task. In this section, we demonstrate the method by studying the physical model of gate-defined quantum dots and superconducting transmon qubits.

Without loss of generality, the simulated gate time for all the RCPs is set to be  $\tau = 50$  ns. The realistic gate time can be arbitrary and we can always rescale the RCPs in the time domain and maintain their robustness. This is guaranteed by the geometric correspondence since the substitution of  $t \rightarrow \alpha t$ ,  $\Omega \rightarrow \Omega/\alpha$  only rescales the length of the error curve and does not change the correspondence such as Eq. (9), as well as the unit-speed properties and robustness conditions of the error curves. In Appendix B, we demonstrate this property and provide the parameters for the RCPs involved in the manuscript.

##### A. Gate-defined quantum dot qubit

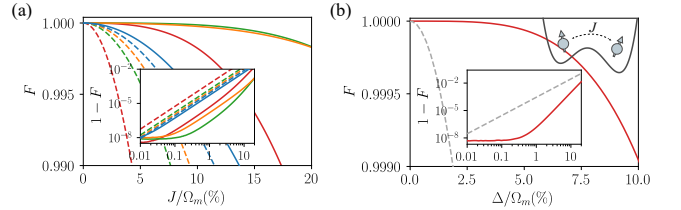


FIG. 6. (a) Fidelities of single-qubit gate  $\{X_\pi, X_{\pi/4}, X_{\pi/2}, X_{2\pi}\}$  (blue, orange, green, red) by RCPs (solid lines) and their cosine counterparts (dashed lines) versus the relative strength of the unwanted coupling  $J$ . (b) Fidelities of  $\sqrt{\text{SWAP}}$  gate by  $R_{1;\perp}^{5\pi/2}$  pulse (red) and cosine pulse (grey) versus the Zeeman difference.

First, we consider gate defined double quantum dot system, in which the spin states of electrons serve as qubit [10, 44–47]. The Hamiltonian is

$$H = \mathbf{B}_1 \cdot \mathbf{S}_1 + \mathbf{B}_2 \cdot \mathbf{S}_2 + J(\mathbf{S}_1 \cdot \mathbf{S}_2 - 1/4), \quad (21)$$

where  $\mathbf{S}_j = (\sigma_{x,j}, \sigma_{y,j}, \sigma_{z,j})/2$  and  $\mathbf{B}_j = (B_{x,j}, B_{y,j}, B_{z,j})$  are the spin operators and magnetic field acting on qubit  $j$ ,  $J$  is the exchange interaction between the spins. We denote the difference of Zeeman

splitting between the two qubits as  $\Delta = B_{z,2} - B_{z,1}$ . Detuning noise from magnetic fluctuations, spin-orbital interaction and residual exchange interaction is one of the major obstacles to further improving the coherence and gate fidelity of such qubits [10, 48].

*Single-qubit robust gates.*—A single QD is a good two-level system. With detuning noise coupled to a driven QD, the system Hamiltonian takes the same form as Eq. (20). Therefore, the robustness of the pulses driving a single QD can be well described by Fig. 4.

Another source of single-qubit errors is the unwanted coupling between two QDs. The Hamiltonian of such a system with Heisenberg interaction takes the form of Eq. (21). Ideally, the universal single-qubit gates  $\{X_\pi, X_{\pi/4}, X_{\pi/2}, X_{2\pi}\}$  on the second qubit are given by  $I \otimes X_\theta$ , as the operations on the second qubit shall not affect the first qubit. It is reasonable to assume  $J \ll \Delta$ , but  $J$  cannot be completely turned off during the single-qubit operations by tuning the gate voltage between two QDs [10]. In the eigenbasis, the two subspaces span $\{|\uparrow\uparrow\rangle, |\uparrow\downarrow\rangle\}$  and span $\{|\downarrow\downarrow\rangle, |\downarrow\uparrow\rangle\}$  both correspond to the second qubit but are detuned by  $J$  in the rotating frame. We tune a magnetic drive  $B_{x,2}(t)$  according to the first order RCPs to implement robust X rotations against this detuning resulting from the unwanted coupling. The numerical results demonstrating robust  $\{X_\pi, X_{\pi/4}, X_{\pi/2}, X_{2\pi}\}$  gates in such double QD system with  $\Delta = 250$  MHz are shown in Fig. 6(a). Although what we demonstrated here is a partial error cancellation since there is an additional crosstalk error between the two subspaces, which will reduce the gate robustness to some extent, the fidelities are still significantly improved in comparison with the cosine waveform. Further, the crosstalk error can be canceled by appropriately timing and implementing additional correction pulses according to [47, 49], or with more sophisticated RCPs.

*Two-qubit robust gates.*—Two-qubit  $\sqrt{\text{SWAP}}$  gate is commonly used as the entangling gates in the QD system. A perfect  $\sqrt{\text{SWAP}}$  can be realized by switching on the exchange coupling in the region where two QDs have zero Zeeman difference—a condition hardly met in experiment either due to the detuning noise or the need of qubit addressability. Note that the entangling originates from the Heisenberg interaction and the Hamiltonian Eq. (21) in the anti-parallel spin states subspace span $\{|\uparrow\downarrow\rangle, |\downarrow\uparrow\rangle\}$  takes the form

$$H(t) = \frac{1}{2} \begin{pmatrix} -J(t) + \Delta & J(t) \\ J(t) & -J(t) - \Delta \end{pmatrix}. \quad (22)$$

To implement a  $\sqrt{\text{SWAP}}$  gate means to control  $J(t)$  to implement  $X_{\pi/2}$  operation in this subspace. The waveform of  $J(t)$  could be upgraded to a robust pulse  $R_{1,\perp}^{5\pi/2}$  in order to fight against the finite Zeeman difference. We numerically solve the time-dependent Schrodinger equation and obtain the results shown in Fig. 6. The robust  $\sqrt{\text{SWAP}}$  gate exhibits a high-fidelity plateau, and the infidelity is several orders of magnitude lower than the cosine pulse counterpart in a wide detuning region.

## B. Transmon qubit

*Single-qubit gates robust to frequency variation.*—For a single superconducting transmon with qubit frequency variation, we use the RCPs  $\{R_1^\pi, R_1^{7\pi/4}, R_1^{5\pi/2}, R_1^{2\pi}\}$  found in Fig. 4 to implement robust single-qubit gates  $\{X_\pi, X_{\pi/4}, X_{\pi/2}, X_{2\pi}\}$ . A transmon is usually considered as a three-level system with a moderate anharmonicity between the first and second transitions [50, 51]. With the transverse control field, a transmon could be modeled as

$$H = (\omega + \delta)a^\dagger a + \frac{u}{2}a^\dagger a^\dagger a a + H_c(t). \quad (23)$$

where the control Hamiltonian [51]

$$H_c(t) = \frac{1}{2}\xi(t)ae^{i\omega_d t} - h.c. \quad (24)$$

The lowest two levels forms the qubit. Here  $\omega$ ,  $u$ ,  $a^\dagger$ ,  $a$  are the qubit frequency, the anharmonicity, the creation and annihilation operators of the transmon.  $\omega_d$  is the frequency of the driving and  $\xi(t)$  is the total control waveform. We apply our theory to the dynamics associated with the qubit levels to correct the errors result from frequency variation, and use DRAG to suppress the leakage to higher level [52]. So  $\xi(t)$  is a sum of RCP  $\Omega(t)$  and the corresponding DRAG pulse  $i\alpha\dot{\Omega}(t)$ . The DRAG parameter  $\alpha$  is related to the transmon anharmonicity [52] and takes the numerically optimized value at zero detuning in our simulation.

We set the gate times for  $\{X_\pi, X_{\pi/4}, X_{\pi/2}, X_{2\pi}\}$  to be 70, 50, 80 and 55 ns, and fix the maximal pulse amplitude  $\Omega_m/2\pi$  to be around 27 MHz. Like previous sections, we use cosine pulses with the same maximal amplitudes for comparison. Our numerical results in Fig. 7(b) illustrate the fidelity plateau over a few MHz of frequency variation for our robust gates. Note that the centers of the fidelity plateau all shift to the left. We conclude the reason to be the AC-Stark shifts associated with the higher levels.

*Single-qubit gates robust to unwanted coupling.*—In realistic multi-qubit systems, a transmon is unavoidably coupled to other quantum systems, the so-called spectators [35, 36, 53–57]. This results in qubit frequency splittings or spectrum broadening, giving rise to correlated errors, which becomes a major obstacle for large-scale quantum computing [36]. As a demonstrative example, we consider two directly-coupled transmon qubits (one spectator and one target qubit) with the Hamiltonian

$$H_0 = \sum_{j=1,2} [\omega_j a_j^\dagger a_j + \frac{u_j}{2} a_j^\dagger a_j^\dagger a_j a_j] + g(a_1^\dagger a_2 + a_1 a_2^\dagger), \quad (25)$$

where  $\omega_j$  is the qubit frequency,  $u_j$  is the anharmonicity for the  $j$ th qubit and  $g$  is the interaction strength. Denote the eigenstates of the spectator-target qubit system [35] as  $|S, T\rangle$ . Up to the second order perturbation, the effective diagonal Hamiltonian in the subspace  $\{|00\rangle, |01\rangle\}$  and  $\{|10\rangle, |11\rangle\}$  is detuned by  $\delta_{zz}$  with



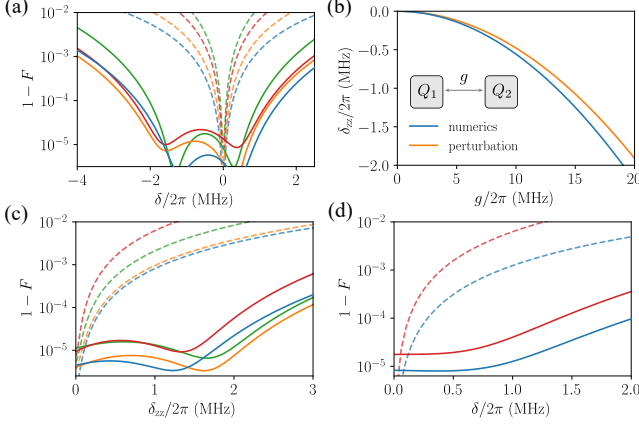


FIG. 7. (a) Fidelities of single qubit gates  $\{X_\pi, X_{\pi/4}, X_{\pi/2}, X_{2\pi}\}$  (blue, orange, green, red) for a transmon qubit by RCPs (solid) and their cosine counterparts (dashed) versus qubit frequency variation. (b) The strength of ZZ-coupling  $\delta_{zz}$  for two capacitively interacting transmons solved numerically (blue) and analytically using perturbation theory (orange).  $g$  is the unwanted interaction strength. (c) Fidelities of single-qubit gates  $\{X_\pi, X_{\pi/4}, X_{\pi/2}, X_{2\pi}\}$  (blue, orange, green, red) for  $Q_2$  by robust pulses (solid) and their cosine counterparts (dashed) versus residual ZZ-coupling strength caused by unwanted interaction  $g$ . (d) Fidelity of two-qubit iSWAP (blue) and  $\sqrt{i}$ SWAP (red) for two coupled transmon qubits by RCPs (solid) and their cosine counterparts (dashed) versus the qubits' frequency difference.

$\delta_{zz} = -\frac{2g^2(u_1+u_2)}{(u_1+\Delta)(u_2-\Delta)}$  and  $\Delta = \omega_2 - \omega_1$ . This detuning  $\delta_{zz}$  is known as the residual ZZ-coupling. We take  $\omega_1/2\pi = 5.0$  GHz,  $\omega_2/2\pi = 5.5$  GHz,  $u_1/2\pi = -0.23$  GHz,  $u_2/2\pi = -0.26$  GHz. The exact  $\delta_{zz}$  obtained by numerical diagonalization and the perturbative one are plotted in Fig. 7(b), as a demonstration of the effectiveness for the perturbative treatment of  $\delta_{zz}$  at small  $g$ . Our numerical results shown in Fig. 7(c) illustrate a significant improvement of gate infidelity in the presence of residual ZZ-coupling up to the order of MHz. When ZZ-coupling is vanishing, the infidelity of robust gates remains of the same order as trivial pulses. Here the DRAG control [52] is added as well.

*Two-qubit gates.* iSWAP gate is one of the favorable two-qubit entangling gates for quantum computing using transmons [1]. Traditional implementation of iSWAP gate requires the two qubits to be on resonance. This could be achieved by tuning qubit frequencies, which, however, induces extra flux noise and hence variation in qubit frequency. To better tune the interaction strength, recent architecture favors tunable couplers [58, 59]. This doesn't change the effective Hamiltonian in Eq. 25, only enabling the control of the coupling strength  $g(t)$ . To correct the error due to the uncertain frequency difference  $\delta$  between the two transmons, we apply RCPs  $\{R_1^\pi, R_1^{5\pi/2}\}$  on  $g(t)$  to implement the robust iSWAP and  $\sqrt{i}$ SWAP gates. We use the qubit settings as in previous discussion to study the variation of gate infidelities versus

$\delta$ . The additional ZZ-coupling induced by higher levels of the transmons when activating the iSWAP interaction is omitted in our simulation as it can be cancelled by exploiting the tunable coupler and setting a proper gate time [60]. Our numerical results shown in Fig. 7(d) demonstrate a great advantage of RCPs over their cosine counterparts. This control scheme also illustrates great potential to simplify the experimental tune-ups of qubit frequencies.

## V. CONCLUSION AND DISCUSSION

Simple and elegant theory with minimum free parameters is a pursuit for scientists. John von Neumann famously said: With four parameters I can fit an elephant, and with five I can make him wiggle his trunk [61, 62].

In this manuscript, we achieve quantum control with different level of robustness using the simplest control waveforms that consist of only one to four cosine functions. This is made possible by utilizing the geometric correspondence between noisy quantum driven evolution and the Frenet-Serret space curves to construct a robust control theory, which provides an experimental-friendly pulse construction framework as a fusion of analytic and numerical approaches. The theory provides explicit conditions of the robustness and correctable errors, as well as a geometric robustness measure for arbitrary control pulses. The framework provides control pulses consisted of very few numbers of Fourier series and robust to noises coupled in arbitrary channel. The duration of the resulting robust control pulse is flexibly adjustable while maintaining robustness. This framework has been applied to construct universal robust quantum gates based on realistic model for semiconductor spin qubits and superconducting transmon qubits, demonstrated with promising numerical results that hit fault-tolerance threshold over a broad robust plateau. Although our discussion in this manuscript focus on single- and two-qubit systems as well as quasi-static noises, this framework could be easily generalized to multi-qubit systems with complex, time-dependent noise via higher-dimensional geometric correspondence and error curve with varying speed. Because of the explicit and general protocol, our theory could be applied on experiments immediately and could be adopted on various physical systems.

## ACKNOWLEDGMENTS

We thank Yu He, Fei Yan for suggestions on the simulations of realistic model and Qihao Guo, Yuanzhen Chen for fruitful discussions. This work was supported by the Key-Area Research and Development Program of Guang-Dong Province (Grant No. 2018B030326001), the National Natural Science Foundation of China (U1801661), the Guangdong Innovative and Entrepreneurial Research Team Program

(2016ZT06D348), the Guangdong Provincial Key Laboratory (Grant No.2019B121203002), the Natural Science Foundation of Guangdong Province (2017B030308003), and the Science, Technology, and Innovation Commission of Shenzhen Municipality (JCYJ20170412152620376, KYTDPT20181011104202253), and the NSF of Beijing (Grants No. Z190012), Shenzhen Science and Technology Program (KQTD20200820113010023).

### AUTHOR CONTRIBUTIONS

XHD conceived and oversaw the project. YJH and XHD derived the theory, designed the protocols, and wrote the manuscript. YJH did all the coding and numerical simulation. JL and JZ gave some important suggestions on the algorithm. All authors contributed to the discussions.

### Appendix A: Geometric Correspondence

Without loss of generality, we first derive the geometric correspondence given by z error curve discussed in the main text. The Hamiltonian in the interaction picture and the error curve are

$$H_I(t) = \delta U_0^\dagger(t) \sigma_z U_0(t) = \mathbf{T} \cdot \hat{\boldsymbol{\sigma}} \quad (\text{A1})$$

$$\mathbf{r}(t) \cdot \hat{\boldsymbol{\sigma}} = \int_0^t U_0^\dagger(t_1) \sigma_z U_0(t_1) dt_1.$$

This noise term  $\delta$  is treated as static perturbation, which agrees with the physical picture where the duration of a quantum gate is much shorter than the time scale of most of the pink noise or decoherence. Note  $\dot{\mathbf{r}}(t) = \mathbf{T}$  is a unit tangent vector, one can then obtain a new unit vector  $\mathbf{N}$  perpendicular to  $\mathbf{T}$  through

$$\begin{aligned} \dot{\mathbf{T}}(t) \cdot \hat{\boldsymbol{\sigma}} &= iU_0^\dagger(t)[H_0(t), \sigma_z]U_0(t) \\ &= \Omega(t)U_0^\dagger(t)(-\sin \Phi(t)\sigma_x + \cos \Phi(t)\sigma_y)U_0(t) \\ &= \Omega(t)\mathbf{N} \cdot \hat{\boldsymbol{\sigma}}. \end{aligned} \quad (\text{A2})$$

The third vector  $\mathbf{B}$  perpendicular to  $\mathbf{T}$  and  $\mathbf{N}$  is given by  $\mathbf{B} = \mathbf{T} \times \mathbf{N}$ ,

$$\mathbf{B}(t) \cdot \hat{\boldsymbol{\sigma}} = U_0^\dagger(t)(-\cos \Phi(t)\sigma_x - \sin \Phi(t)\sigma_y)U_0(t). \quad (\text{A3})$$

It's time derivative satisfies

$$\begin{aligned} \dot{\mathbf{B}}(t) \cdot \hat{\boldsymbol{\sigma}} &= \dot{\Phi}U_0^\dagger(t)(\sin \Phi(t)\sigma_x - \cos \Phi(t)\sigma_y)U_0(t) \\ &= -\dot{\Phi}(t)\mathbf{N} \cdot \hat{\boldsymbol{\sigma}}. \end{aligned} \quad (\text{A4})$$

The three unit vectors  $\{\mathbf{T}, \mathbf{N}, \mathbf{B}\}$ , as tangent, normal, and binormal unit vectors of the error curve formed a Frenet-Serret frame and their defining formulas Eq. (8) are directly follows from Eq. (A2)-(A3). They satisfy the Frenet-Serret equations

$$\begin{pmatrix} \dot{\mathbf{T}} \\ \dot{\mathbf{N}} \\ \dot{\mathbf{B}} \end{pmatrix} = \begin{pmatrix} 0 & \kappa & 0 \\ -\kappa & 0 & \tau \\ 0 & -\tau & 0 \end{pmatrix} \begin{pmatrix} \mathbf{T} \\ \mathbf{N} \\ \mathbf{B} \end{pmatrix}, \quad (\text{A5})$$

with  $\Omega(t)$  and  $\dot{\Phi}(t)$  play the role of signed curvature  $\kappa(t)$  and singularity free torsion  $\tau(t)$  of the error curve, as stated in Eq. (9).

Different from standard differential geometry, the Frenet vectors defined physically by Eq. (8) are continuous and differentiable since the pulses are assumed to be continuous and differentiable. We call the signed curvature as the projection of the curvature vector  $\dot{\mathbf{T}}$  onto the normal vector  $\mathbf{T} \cdot \mathbf{N} = \kappa$ . It can take negative values since the corresponding pulse amplitude  $\Omega$  can be negative. It relates to the conventional curvature in standard differential geometry of curves by taking the absolute value. The torsion defined by  $\dot{\mathbf{B}} \cdot \mathbf{N} = -\tau$  is also continuous and does not have singularity at curvature zero point as in standard differential geometry. This mathematical ambiguity is addressed in Appendix C.

One can also establish the geometric correspondence by error curve in other directions. Here we take x error curve as an example. The x- error curve is given by  $\dot{\mathbf{r}} = U_0^\dagger \sigma_x U_0$ , and the Frenet vectors are defined as

$$\begin{aligned} \mathbf{T} \cdot \hat{\boldsymbol{\sigma}} &= U_0^\dagger(t) \sigma_x U_0(t) \\ \mathbf{N} \cdot \hat{\boldsymbol{\sigma}} &= -U_0^\dagger(t) \sigma_z U_0(t) \\ \mathbf{B} \cdot \hat{\boldsymbol{\sigma}} &= U_0^\dagger(t) \sigma_y U_0(t). \end{aligned} \quad (\text{A6})$$

The relation between control pulses and the curvature-torsion of x- error curve are given by

$$\begin{aligned} \kappa(t) &= \dot{\mathbf{T}} \cdot \mathbf{N} = \Omega(t) \sin \Phi(t) \\ \tau(t) &= -\dot{\mathbf{B}} \cdot \mathbf{N} = \Omega(t) \cos \Phi(t). \end{aligned} \quad (\text{A7})$$

Imposing robustness constraint on this error curve will lead to the dynamics robust against x error.

### Appendix B: Supplementary for numerical results

As an additional assessment of the robustness of our RCPs presented in Sec. (III), we calculate the Magnus expansion coefficients up to fourth order numerically. The rescaled Magnus coefficients  $\bar{A}_n = 10^{-n}||A_n||$  of the  $X_{\pi/4}$  gate evolution produced by the  $R_{1;\perp}^{\pi/4}$ ,  $R_{2;\perp}^{\pi/4}$ ,  $R_{\text{ex};\perp}^{\pi/4}$  and cosine pulse are plotted in Fig. 8 for comparison, where  $R_{1;\perp}^{\pi/4}$  and  $R_{\text{ex};\perp}^{\pi/4}$  are RCPs obtained by our pulse generation protocol and  $R_{2;\perp}^{\pi/4}$  is a RCP with second order robustness constructed from analytical plane curve in appendix D.

Compared with cosine pulse,  $R_{1;\perp}^{\pi/4}$  and  $R_{2;\perp}^{\pi/4}$  has small Magnus coefficients up to first and second order respectively, while all four coefficients for  $R_{\text{ex};\perp}^{\pi/4}$  pulse are significantly suppressed, indicating its higher robustness.

Our robust control pulses are suitable for different gate time, and the pulse rescaling in the time domain does not change their robustness since the substitution  $t \rightarrow \alpha t$ ,  $\Omega \rightarrow \Omega/\alpha$  does not change Eq. (9) and thus maintains the geometric correspondence between pulses and their error curves. Here we present a 50 ns pulse for  $3\pi/2$  rotation

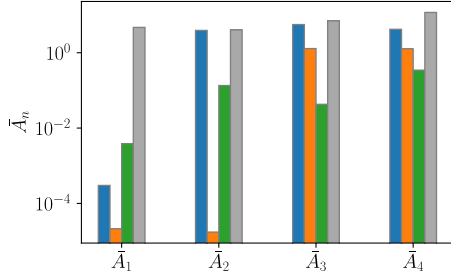


FIG. 8. Numerical certification of robust pulses. The first to fourth order rescaled Magnus error coefficients for the  $X_{\pi/4}$  gate evolution produced by  $R_{1;\perp}^{\pi/4}$ ,  $R_{2;\perp}^{\pi/4}$ ,  $R_{\text{ex};\perp}^{\pi/4}$  and cosine pulse (blue, orange, green, grey).

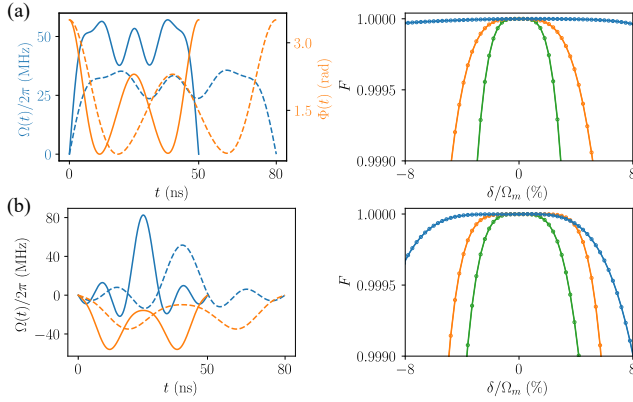


FIG. 9. (a) Left: the  $R_{1;\text{all}}^{3\pi/2}$  pulses with 50 ns duration (solid) and the rescaled pulses with 80 ns duration (dashed). Right: fidelity of the corresponding  $Y_{3\pi/2}$  gate generated by the 50 ns pulses (solid) versus errors  $\delta_z$ ,  $\delta_x$  and  $\delta_y$  (blue, orange and green) respectively and the gate fidelity by 80 ns pulses versus the same errors (circle). (b) Left: the  $R_{1;\text{all}}^{\pi}$  pulses in X-Y driven scheme with 50 ns duration (solid) and the rescaled pulses with 80 ns duration (dashed). Right: fidelity of the corresponding  $Y_{3\pi/2}$  gate generated by the 50 ns pulses (solid) versus errors  $\delta_z$ ,  $\delta_x$  and  $\delta_y$  (blue, orange and green) respectively and the gate fidelity by 80 ns pulses versus the same errors (circle).

around Y axis by adding a  $\pi/2$  phase constant to the RCP  $R_{1;\text{all}}^{3\pi/2}$  presented in the main text and rescale it to an 80 ns pulse. It maintains robustness in three axes with error Hamiltonian in the form of Eq. (4). Fig. 9(a) shows the rescaled pulse and the gate fidelity of the  $Y_{3\pi/2}$  gate generated by the two pulses. The coincide fidelity values versus the relative noise strength demonstrate their same robustness.

In addition, our pulse generation protocol is compatible with direct x-y control scheme, in which the noiseless Hamiltonian is of the form  $H_0(t) = \Omega_x(t)/2\sigma_x + \Omega_y(t)/2\sigma_y$ . Here we present a 50 ns pulse for  $\pi$  rotation around X axis (denoted by  $R_{1;\text{all}}^{\pi}$ ) that has robustness in three axes and rescale it to a 100 ns pulse. Fig. 9(b)

shows the rescaled pulse and the gate fidelity of the  $X_{\pi}$  gate generated by the two pulses.

The parameters of all RCPs presented in the main text and this section are listed in the following Table I.

### Appendix C: From regular space curve to pulse

As mentioned in the main text, one can construct robust control pulses by reverse engineering of space curves because of the geometric correspondence between regular space curves and the dynamics of a two-level system, where the signed curvature and singularity free torsion of the space curves are related to the drive amplitude and phase. However, from the mathematical point of view, it is known that the existence and continuity of the Frenet-Serret frame are not guaranteed in standard differential geometry in the vicinity of curvature-vanishing points since the definition of  $\mathbf{N}$ ,  $\mathbf{B}$  and torsion need the curvature to be non-zero [39, 40]. This singularity and discontinuity issue can be solved in a pure mathematical manner by defining the continuous Frenet-Serret frame vectors in terms of three singularity free Frenet-Euler angles, as introduced in [63]. The corresponding control pulses of the dynamics can be obtained by the resulting signed curvature and singularity free torsion in terms of arc-length variable. We summarize this approach and demonstrate a few examples as follows.

For a regular space curve in arbitrary parametrization  $\mathbf{r}(\lambda)$ . The unit tangent vector  $\mathbf{T}$  can always be written in terms of two angles by

$$\mathbf{T} = (x', y', z')^T / |\mathbf{r}'| = (\cos \psi \cos \theta, \sin \psi \cos \theta, \sin \theta)^T, \quad (\text{C1})$$

where  $'$  represents derivative with respect to  $\lambda$  and angles  $\psi$  and  $\theta$  are determined by derivatives of the curve coordinate.

The existence of well-defined normal vectors relies on the third angle  $\phi$  defined as

$$\tan \phi = -\frac{(z''(x'^2 + y'^2) - z'(x'x'' + y'y''))}{|\mathbf{r}'|(y''x' - x''y')}. \quad (\text{C2})$$

At curvature-zero point, where  $\kappa = x'' = y'' = z'' = 0$ , it is still well-defined by taking limit according to L'Hospital rule.

The other two vector of the coordinate system are then expressed as

$$\mathbf{N} = \begin{pmatrix} -\sin \psi \cos \phi + \cos \psi \sin \theta \sin \phi \\ \cos \psi \cos \phi + \sin \psi \sin \theta \sin \phi \\ -\cos \theta \sin \phi \end{pmatrix} \quad (\text{C3})$$

and

$$\mathbf{B} = \begin{pmatrix} -\sin \psi \sin \phi - \cos \psi \sin \theta \cos \phi \\ \cos \psi \sin \phi - \sin \psi \sin \theta \cos \phi \\ \cos \theta \cos \phi \end{pmatrix}. \quad (\text{C4})$$

| RCPs                           |            | $a$                                 | $\phi$                        |
|--------------------------------|------------|-------------------------------------|-------------------------------|
| $R_{1;\perp}^\pi$              | $\Omega$   | [0.010, -0.259, -0.033]             | [-0.015, -0.038]              |
| $R_{1;\perp}^{7\pi/4}$         | $\Omega$   | [0.223, 0.134, 0.076]               | [0.001, -0.020]               |
| $R_{1;\perp}^{5\pi/2}$         | $\Omega$   | [0.349, 0.307]                      | [-0.003]                      |
| $R_{1;\perp}^{2\pi}$           | $\Omega$   | [0.258, 0.183]                      | [0]                           |
| $R_{\text{ex};\perp}^\pi$      | $\Omega$   | [-0.328, -1.014, -1.195, -0.304]    | [-0.003, -0.003, -0.008]      |
| $R_{\text{ex};\perp}^{9\pi/4}$ | $\Omega$   | [0.147, -0.089, -0.613, -0.161]     | [-0.0123, -0.061, -0.073]     |
| $R_{\text{ex};\perp}^{5\pi/2}$ | $\Omega$   | [0.241, 0.084, -0.482, -0.036]      | [-0.036, 0.014, 0.107]        |
| $R_{\text{ex};\perp}^{2\pi}$   | $\Omega$   | [0.042, -0.290, -0.765, -0.274]     | [0.003, 0.003, 0.003]         |
| $R_{1;\text{all}}^{3\pi/2}$    | $\Omega$   | [0.624, 0.484, 0.193, 0.070, 0.073] | [0.005, 0.013, 0.003, -0.070] |
| $R_{1;\text{all}}^\pi$         | $\Phi$     | [0.083, 0.362, 1.174, 0.237, 0.074] | [0.022, 0.017, 0.011, -0.037] |
| $R_{1;\text{all}}^\pi$         | $\Omega_x$ | [0.007, -0.236, 0.032, -0.250]      | [0.008, -0.601, -0.029]       |
|                                | $\Omega_y$ | [-0.327, -0.127, 0.167, 0.066]      | [0.035, -0.079, -0.096]       |

TABLE I. Parameters for RCPs, gate time  $T = 50$  ns, amplitude unit GHz.

Here the three angles  $\{\psi, \theta, \phi\}$ , named Frenet angles, are used to define curve geometry and resolve the ambiguity at curvature-vanishing points. We refer to [63] for a detailed discussion of this choice of coordinate system. According to the Frenet equation, the signed curvature and singularity free torsion are obtained from the continuous Frenet vectors by

$$\begin{aligned}\kappa(\lambda) &= \frac{\mathbf{T}' \cdot \mathbf{N}}{\|\mathbf{r}'\|} \\ \tau(\lambda) &= -\frac{\mathbf{B}' \cdot \mathbf{N}}{\|\mathbf{r}'\|}.\end{aligned}\quad (\text{C5})$$

The geometric correspondence with z error curve given by Eq. (8) and the above mentioned mathematically non-singular frame choice can be connected as follows. Consider a conventional parametrization of evolution unitary by

$$\begin{aligned}U_0(t) &= \begin{pmatrix} u_1(t) & -u_2^*(t) \\ u_2(t) & u_1^*(t) \end{pmatrix} \\ u_1(t) &= e^{\frac{1}{2}i(\psi_1(t)+\phi_1(t))} \cos\left(\frac{\theta_1(t)}{2}\right) \\ u_2(t) &= -ie^{\frac{1}{2}i(\psi_1(t)-\phi_1(t))} \sin\left(\frac{\theta_1(t)}{2}\right).\end{aligned}\quad (\text{C6})$$

By equating the Frenet vectors defined by Eq. (C1)-(C4) and Eq. (8) with the unitary parametrization of Eq. (C6) we have the following relations of angles

$$\begin{aligned}\psi_1 &= \psi - \frac{\pi}{2} \\ \theta_1 &= \frac{\pi}{2} - \theta \\ \phi_1 + \Phi &= \frac{\pi}{2} - \phi.\end{aligned}\quad (\text{C7})$$

As indicated in [31], the initial condition of the ideal evolution and the target gate unitary at the given gate

time  $T$  set the boundary conditions of these angles. Note that  $U_0(0) = I$  gives the initial conditions  $\theta_1(0) = 0$  and  $\psi_1(0) = -\phi_1(0)$ . Since  $H_0(t) = i\dot{U}_0(t)U_0^\dagger(t)$ , we have

$$(i\dot{\psi}_1 \sin \theta_1 + \dot{\theta}_1)e^{-i\phi_1} = \Omega(t)e^{i\Phi}$$

and  $\Phi(0) = -\phi_1(0) = \psi_1(0)$ . The final  $\theta_1(T)$  and  $\psi_1(T)$  correspond to the final time tangent vector  $\mathbf{r}(T)$  and  $\phi_1(T)$  is related to the total torsion

$$\phi_1(T) - \phi_1(0) = -\int_0^T \tau(t)dt - \arg[i\dot{\psi}_1 \sin \theta_1 + \dot{\theta}_1]_0^T.$$

Having established the correspondence from space curve to control pulse, we further elucidate this correspondence by constructing robust control pulses with the following examples of space curves. First, for a unit-speed space curve

$$\mathbf{r}(t) = \begin{pmatrix} (1 + \cos \frac{t}{2}) \cos \frac{t}{2} \\ (1 - \cos \frac{t}{2}) \sin \frac{t}{2} \\ \frac{4}{3} \sin \frac{3t}{4} \end{pmatrix}$$

with  $t \in [0, 4\pi]$ . Note that in the context of curve geometry, we refer to  $t$  as the curve length variable. One can determine the Frenet angles unambiguously from the tangent vector and Eq. (C1) to obtain  $\theta = -3t/4 + \pi/2$ ,  $\psi = -t/4 + \pi$  and  $\tan \phi = -3/\sin(3t/4)$ . Then vectors  $\mathbf{N}$  and  $\mathbf{B}$  can be obtained straightforwardly and the curvature and torsion are given by

$$\begin{aligned}\kappa(t) &= \frac{1}{8} \sqrt{38 - 2 \cos \frac{3t}{2}} \\ \tau(t) &= \frac{-73 \cos \frac{3t}{4} + \cos \frac{9t}{4}}{-152 + 8 \cos \frac{3t}{2}}.\end{aligned}$$

The corresponding pulses obtained from this curve via the correspondence Eq. (9) are shown in Fig. 10(a). It

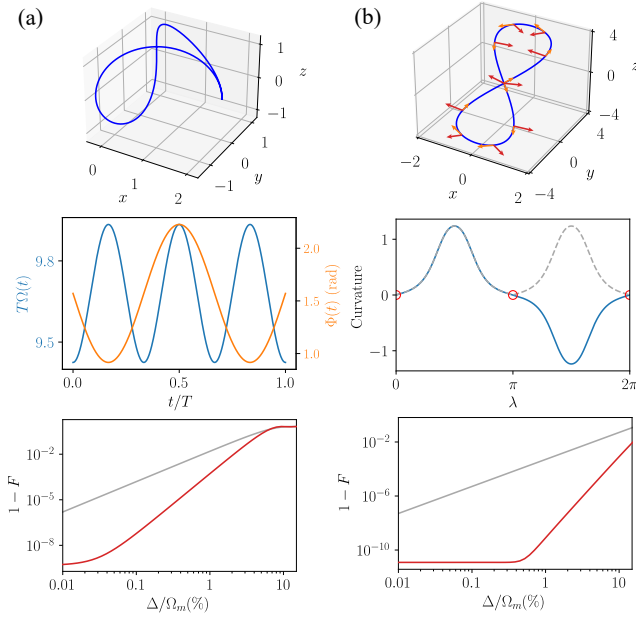


FIG. 10. (a) A space curve (up), the corresponding RCP (middle) and the fidelity of  $X_\pi$  gate performed by the RCP (red) and its cosine pulse counterpart (grey) versus detuning noise (down). (b) A figure 8 space curve with its tangent and continuous normal vectors marked by the orange and red arrows (up); the curvature (dashed grey) and signed curvature (blue) of this curve (middle). The curvature zero points are marked by red circles; The fidelity of  $X_{2\pi}$  gate performed by the RCP obtained from this curve (red) and its cosine pulse counterpart (grey) versus detuning noise (right).

generates a  $\pi$  rotation if we choose an initial phase  $\pi/2$  as the integral constant of  $\Phi$ . The robustness of  $X_\pi$  gate performed by them against detuning noise are also shown in Fig. 10(a).

Specifically, for plane curve, we have  $\theta = \phi = 0$ ,  $\mathbf{T} = (\cos \psi, \sin \psi, 0)^T$  and  $\mathbf{N} = (-\sin \psi, \cos \psi, 0)^T$  with  $\cos \psi = x'/\sqrt{x'^2 + y'^2}$  and  $\sin \psi = y'/\sqrt{x'^2 + y'^2}$ . In this case, the normal vector are well-defined regardless of the existence of curvature zero. According to and Eq. (C5), the signed curvature of plane curve is given by

$$\kappa(\lambda) = \frac{x'y'' - y'x''}{(x'^2 + y'^2)^{3/2}}. \quad (\text{C8})$$

Consider  $\mathbf{r}(\lambda) = (\sin 2\lambda, 3.5 \sin \lambda, 0)$  with  $\lambda \in [0, 2\pi]$  as an example, we have  $\kappa(\lambda) = (10.5 \sin \lambda + 3.5 \sin 3\lambda)/\|\mathbf{r}'\|^3$  with  $\|\mathbf{r}'\| = (12.25 \cos^2 \lambda + 4 \cos^2 2\lambda)^{1/2}$ . To obtain the corresponding pulse, we perform a numerical variable transformation to obtain the curvature in terms of curve length variable  $t$ , i.e.,  $\Omega(t) = \kappa(t)$ . A systematic construction of the first and second order robust control pulses from analytical plane curves are discussed in the next section.

To demonstrate a space curve with curvature zeros, we take a figure 8 space curve shown in Fig. 10(b)  $\mathbf{r}(\lambda) = (\sin 2\lambda, 3.5 \sin \lambda, 3.5 \sin \lambda)$  with  $\lambda \in [0, 2\pi]$  for example.

We have  $\sin \psi = \sin \theta = 3.5 \cos \lambda / \|\mathbf{r}'\|$  and  $\tan \psi = -2 \cos 2\lambda / \|\mathbf{r}'\|$  with  $\|\mathbf{r}'\| = (24.5 \cos^2 \lambda + 4 \cos^2 2\lambda)^{1/2}$ . At the point of curvature singularity  $t = \pi$ ,  $\tan \phi$  is still well-defined by taking limit of Eq. (C2). The continuous tangent and normal vector are illustrated using arrows on the space curve. The conventional curvature and signed curvature are defined by  $\|\mathbf{r}' \times \mathbf{r}''\|/\|\mathbf{r}'\|^3$  and Eq. (C5) in terms of curve coordinates and the continuous Frenet vectors respectively and are plotted in Fig. 10(b) for comparison. The curvature zero at  $t = \pi$  will lead to a singularity and discontinuity of the normal vector and torsion in the framework of standard differential geometry of space curves, while their counterparts obtained by the Frenet angles is continuous and singularity free. The corresponding robust pulses is given by the signed curvature and singular free torsion ( $\tau(\lambda) = 0$  for this example) obtained from the continuous Frenet vectors (Eq. (C5)). The robust pulse performs an identity operation and its robustness against detuning noise are presented in Fig. 10(b).

#### Appendix D: Robust Pulses from Analytical Construction of Plane Curves

In this section, we construct a set of first and second order RCPs against longitudinal error from analytical plane curves that are closed and with zero net-area, which are z error curve of the corresponding dynamics satisfying the first and second order robustness condition.

First or all, a series of first order RCPs can be generated from the modified half lemniscates of Bernoulli used in [14]

$$\begin{aligned} x_1(\lambda) &= \frac{\alpha \sin(2\lambda)}{3 + \cos(2\lambda)} \\ y_1(\lambda) &= \frac{2 \sin(\lambda)}{3 + \cos(2\lambda)}. \end{aligned} \quad (\text{D1})$$

When  $0 \leq \lambda \leq \pi$ , it becomes closed curve that subtends an angle  $\theta = \pi - 2 \arctan(\frac{1}{\alpha})$  at the origin. The rotation angle of the corresponding pulse is given by the total curvature or total winding angle of the tangent vector of the curve  $\phi = \int_0^\pi dt \kappa(\lambda) = 2\pi - 2 \arctan(\frac{1}{\alpha})$ . Thus, through tuning  $\alpha$ , one can obtain the curves for first order RCPs with rotational angle  $\pi < \phi < 2\pi$ . In addition, the curve for  $\pi$  pulse can be obtained by multiplying  $x_1(\lambda)$  by a power of  $\sin(\lambda)$  to diminish the angle subtended at the origin and guarantee the curvature starts and ends at zero. A first order  $2\pi$  pulse can be constructed from a modified circle.

We construct four plane curves for first order RCPs  $\{R_{1',\perp}^\pi, R_{1',\perp}^{7\pi/4}, R_{1',\perp}^{5\pi/2}, R_{1',\perp}^{2\pi}\}$ . The analytical expressions of the plane curves are listed in Table. II, and the corresponding RCPs are obtained by the calculating their curvature in the unit-speed parametrization. The four first order RCPs and the corresponding plane curves are shown in Fig. 11(a).

We then present a piecewise construction of the plane curves for second order RCPs with rotation angle  $0 <$

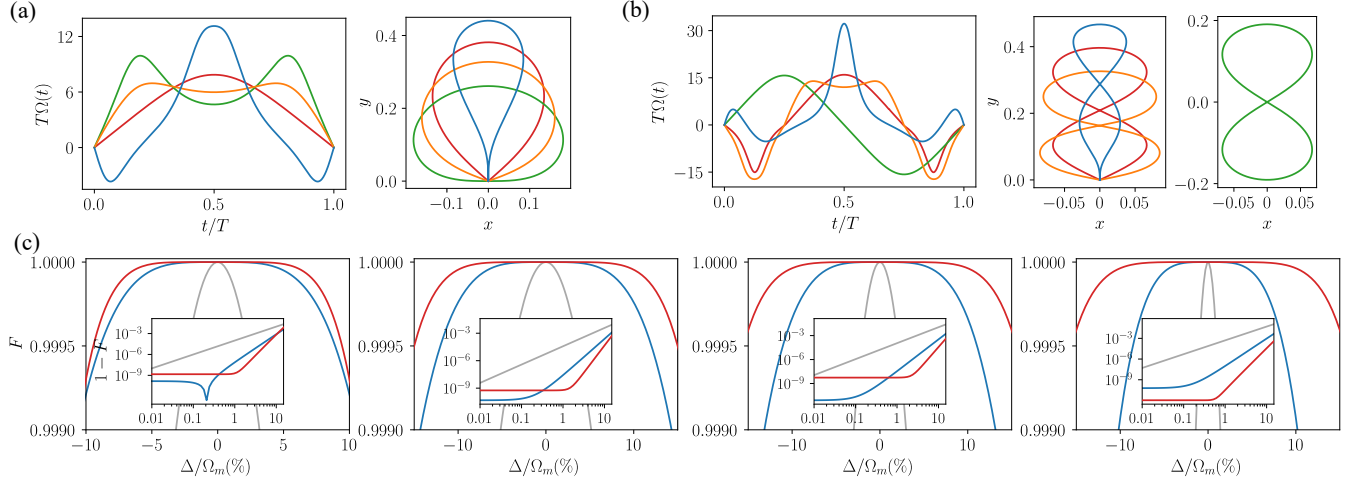


FIG. 11. (a) First order robust control pulses  $\{R_{1';\perp}^\pi, R_{1';\perp}^{7\pi/4}, R_{1';\perp}^{5\pi/2}, R_{1';\perp}^{2\pi}\}$  (left) obtained from analytical plane curves (right). (b) Second order robust control pulses  $\{R_{2;\perp}^\pi, R_{2;\perp}^{7\pi/4}, R_{2;\perp}^{5\pi/2}, R_{2;\perp}^{2\pi}\}$  (left) obtained from analytical plane curves (right). (c) Fidelity of four single-qubit gates  $\{X_\pi, X_{\pi/4}, X_{\pi/2}, X_{2\pi}\}$  (left to right) realized by the second order, first order RCPs shown in (b)(a) and their cosine pulse counterpart (red, blue, grey) against detuning noise. Insets: Infidelity versus noise percentage for each gate in log-log scale, which shows polynomial and constant-polynomial increasing trend for cosine pulses and RCPs respectively.

$\phi < \pi$ . The basic constituents of the composite curve are the aforementioned modified Bernulli half lemniscates  $\{x_1(\lambda), y_1(\lambda)\}$  and the sinusoidal curve

$$\begin{aligned} x_2(\lambda) &= \alpha \sin(2\lambda) \\ y_2(\lambda) &= 2\lambda. \end{aligned} \quad (D2)$$

The equation of the composite curve is

$$\begin{cases} x(\lambda) = -\beta x_2(\lambda), y(\lambda) = \beta y_2(\lambda), & 0 \leq \lambda < \frac{\pi}{2} \\ x(\lambda) = x_1(\lambda - \frac{\pi}{2}), y(\lambda) = \beta y_2(\frac{\pi}{2}) + y_1(\lambda - \frac{\pi}{2}), & \frac{\pi}{2} \leq \lambda < \frac{3\pi}{2} \\ x(\lambda) = \beta x_2(2\pi - \lambda), y(\lambda) = \beta y_2(2\pi - \lambda), & \frac{3\pi}{2} \leq \lambda \leq 2\pi \end{cases} \quad (D3)$$

where  $\alpha$  and  $\beta$  are two parameters determined by the target rotation angle  $\phi = 2 \arctan(\frac{1}{\alpha})$  and the zero net-area condition  $\int_0^{2\pi} (y'x - x'y) d\lambda = 0$ .

We construct RCPs  $R_{2;\perp}^{\pi/4}$  and  $R_{2;\perp}^{\pi/2}$  from the composite curve of Eq. (D3), the RCP  $R_{2;\perp}^{\pi/4}$  is obtained by modifying the curves for  $R_{1';\perp}^\pi$  and  $R_{2;\perp}^{2\pi}$  is generated from the curves Eq. (D1) with  $0 \leq \lambda \leq 2\pi$ . The four plane curves and the corresponding second order RCPs are shown in Fig. 11(b), and the analytical expressions for the four constructed curves are listed in Table II.

Fig. 11(c) shows the robustness of the single qubit gate  $\{X_\pi, X_{\pi/4}, X_{\pi/2}, X_{2\pi}\}$  performed by the first and second order RCPs mentioned above against detuning noise. All of the RCPs exhibit robust infidelity plateau with values much smaller than that of the cosine pulse within the noise region from 0.01% to 1%.

- 
- [1] F. Arute, K. Arya, R. Babbush, D. Bacon, J. C. Bardin, R. Barends, R. Biswas, S. Boixo, F. G. Brandao, D. A. Buell, *et al.*, *Nature* **574**, 505 (2019).  
[2] Y. Wu, W.-S. Bao, S. Cao, F. Chen, M.-C. Chen, X. Chen, T.-H. Chung, H. Deng, Y. Du, D. Fan, *et al.*, *Physical review letters* **127**, 180501 (2021).  
[3] S. Krinner, N. Lacroix, A. Remm, A. Di Paolo, E. Genois, C. Leroux, C. Hellings, S. Lazar, F. Swiadek, J. Herrmann, *et al.*, *Nature* **605**, 669 (2022).  
[4] J. Preskill, arXiv preprint arXiv:2208.08064 (2022).  
[5] J. Preskill, *Quantum* **2**, 79 (2018).  
[6] S. J. Glaser, U. Boscain, T. Calarco, C. P. Koch, W. Köckenberger, R. Kosloff, I. Kuprov, B. Luy, S. Schirmer, T. Schulte-Herbrüggen, *et al.*, *The European Physical Journal D* **69**, 1 (2015).  
[7] C. P. Koch, *Journal of Physics: Condensed Matter* **28**, 213001 (2016).  
[8] C. P. Koch, U. Boscain, T. Calarco, G. Dirr, S. Filipp, S. J. Glaser, R. Kosloff, S. Montangero, T. Schulte-Herbrüggen, D. Sugny, *et al.*, arXiv preprint arXiv:2205.12110 (2022).  
[9] R. Barends, J. Kelly, A. Megrant, A. Veitia, D. Sank, E. Jeffrey, T. C. White, J. Mutus, A. G. Fowler, B. Campbell, *et al.*, *Nature* **508**, 500 (2014).  
[10] X. Xue, M. Russ, N. Samkharadze, B. Undseth, A. Sammak, G. Scappucci, and L. M. Vandersypen, *Nature* **601**, 343 (2022).



| RCPs                    | Curve Functions   |
|-------------------------|---|
| $R_{1';\perp}^{3\pi/2}$ | $x(\lambda) = x_1(\lambda) \quad y(\lambda) = y_1(\lambda), \quad \alpha = 1, \quad 0 \leq \lambda \leq \pi$  |
| $R_{2;\perp}^{\pi/2}$   | $x(\lambda) = -\beta x_2(\lambda) \quad y(\lambda) = \beta y_2(\lambda), \quad 0 \leq \lambda < \frac{\pi}{2}$  |
|                         | $x(\lambda) = x_1(\lambda - \frac{\pi}{2}) \quad y(\lambda) = \beta y_2(\frac{\pi}{2}) + y_1(\lambda - \frac{\pi}{2}), \quad \frac{\pi}{2} \leq \lambda < \frac{3\pi}{2}$       |
|                         | $x(\lambda) = \beta x_2(2\pi - \lambda) \quad y(\lambda) = \beta y_2(2\pi - \lambda), \quad \frac{3\pi}{2} \leq \lambda \leq 2\pi$  |
|                         | $\alpha = 1 \quad \beta = 0.3535534$  |
| $R_{1';\perp}^{7\pi/4}$ | $x_{1'}(\lambda) = x_1(\lambda) \quad y_{1'}(\lambda) = y_1(\lambda)(-0.3\lambda(\lambda - \pi) + 1), \quad \alpha = 1, \quad 0 \leq \lambda \leq \pi$                          |
| $R_{2;\perp}^{\pi/4}$   | $x(\lambda) = -\beta x_2(\lambda) \quad y(\lambda) = \beta y_2(\lambda), \quad 0 \leq \lambda < \frac{\pi}{2}$  |
|                         | $x(\lambda) = x_{1'}(\lambda - \frac{\pi}{2}) \quad y(\lambda) = \beta y_2(\frac{\pi}{2}) + y_{1'}(\lambda - \frac{\pi}{2}), \quad \frac{\pi}{2} \leq \lambda < \frac{3\pi}{2}$ |
|                         | $x(\lambda) = \beta x_2(2\pi - \lambda) \quad y(\lambda) = \beta y_2(2\pi - \lambda), \quad \frac{3\pi}{2} \leq \lambda \leq 2\pi$  |
|                         | $\alpha = 2.4142136 \quad \beta = 0.4801245$  |
| $R_{1';\perp}^{\pi}$    | $x_{1'}(\lambda) = x_1(\lambda) \sin^2(\lambda) \quad y_{1'}(\lambda) = y_1(\lambda), \quad \alpha = 0.72, \quad 0 \leq \lambda \leq \pi$                                       |
| $R_{2;\perp}^{\pi}$     | $x(\lambda) = x_{1'}(\lambda)(\lambda - (\frac{\pi}{2} - b))(\lambda - (\frac{\pi}{2} + b)) \quad y(\lambda) = 0.25y_{1'}(\lambda)$   |
|                         | $\alpha = -0.3, b = 0.6100818 \quad 0 \leq \lambda \leq \pi$  |
| $R_{1';\perp}^{2\pi}$   | $x(\lambda) = \frac{2.4 \sin(2\lambda + \pi i)}{2 + \cos 2\lambda} \quad y(\lambda) = \frac{\cos(2\lambda + \pi) + 1}{2 + \cos 2\lambda} \sin(\lambda + \pi)$                   |
| $R_{2;\perp}^{2\pi}$    | $x(\lambda) = x_1(\lambda) \quad y(\lambda) = y_1(\lambda), \quad \alpha = 1, \quad 0 \leq \lambda \leq 2\pi$   |

TABLE II. Plane curve functions for RCPs. Curve ansatz  $\{x_1, y_1\}$  and  $\{x_2, y_2\}$  given by Eq. (D1) and Eq. (D2) are used. For the curve functions of RCPs  $R_{1';\perp}^{7\pi/4}$  and  $R_{1';\perp}^{\pi}$ , additional modifications are made to smoothen the resulting pulses and the modified curve functions (denoted by  $\{x_{1'}, y_{1'}\}$ ) are used in constructing the plane curves for  $R_{2;\perp}^{7\pi/4}$  and  $R_{2;\perp}^{\pi}$  pulses.

- [11] C. Ballance, T. Harty, N. Linke, M. Sepiol, and D. Lucas, *Physical review letters* **117**, 060504 (2016).
- [12] D. Bluvstein, H. Levine, G. Semeghini, T. T. Wang, S. Ebadi, M. Kalinowski, A. Keesling, N. Maskara, H. Pichler, M. Greiner, *et al.*, *Nature* **604**, 451 (2022).
- [13] K. Khodjasteh and L. Viola, *Physical review letters* **102**, 080501 (2009).
- [14] J. Zeng, X.-H. Deng, A. Russo, and E. Barnes, *New Journal of Physics* **20**, 033011 (2018).
- [15] L. Xiang, Z. Zong, Z. Sun, Z. Zhan, Y. Fei, Z. Dong, C. Run, Z. Jia, P. Duan, J. Wu, *et al.*, *Physical Review Applied* **14**, 014099 (2020).
- [16] B. M. Terhal, J. Conrad, and C. Vuillot, *Quantum Science and Technology* **5**, 043001 (2020).
- [17] W. Cai, Y. Ma, W. Wang, C.-L. Zou, and L. Sun, *Fundamental Research* **1**, 50 (2021).
- [18] T. Manovitz, Y. Shapira, L. Gazit, N. Akerman, and R. Ozeri, *PRX quantum* **3**, 010347 (2022).
- [19] Z. Zhou, R. Sitler, Y. Oda, K. Schultz, and G. Quiroz, *arXiv preprint arXiv:2208.05978* (2022).
- [20] N. Khaneja, T. Reiss, C. Kehlet, T. Schulte-Herbrüggen, and S. J. Glaser, *Journal of magnetic resonance* **172**, 296 (2005).
- [21] T. Caneva, T. Calarco, and S. Montangero, *Physical Review A* **84**, 022326 (2011).
- [22] C. Yang, K. Chan, R. Harper, W. Huang, T. Evans, J. Hwang, B. Hensen, A. Laucht, T. Tanttu, F. Hudson, *et al.*, *Nature Electronics* **2**, 151 (2019).
- [23] T. Figueiredo Roque, A. A. Clerk, and H. Ribeiro, *npj Quantum Information* **7**, 1 (2021).
- [24] H. Ribeiro, A. Baksic, and A. A. Clerk, *Physical Review X* **7**, 011021 (2017).
- [25] Y. Song, J. Li, Y.-J. Hai, Q. Guo, and X.-H. Deng, *Physical Review A* **105**, 012616 (2022).
- [26] M. V. Berry, *Proceedings of the Royal Society of London. Series A: Mathematical and Physical Sciences* **430**, 405 (1990).
- [27] C. Zu, W.-B. Wang, L. He, W.-G. Zhang, C.-Y. Dai, F. Wang, and L.-M. Duan, *Nature* **514**, 72 (2014).
- [28] R. Balakrishnan and R. Dandoloff, *European journal of physics* **25**, 447 (2004).
- [29] A. Ekert, M. Ericsson, P. Hayden, H. Inamori, J. A. Jones, D. K. Oi, and V. Vedral, *Journal of modern optics* **47**, 2501 (2000).
- [30] Y. Xu, Z. Hua, T. Chen, X. Pan, X. Li, J. Han, W. Cai, Y. Ma, H. Wang, Y. Song, *et al.*, *Physical Review Letters* **124**, 230503 (2020).
- [31] J. Zeng, C. Yang, A. Dzurak, and E. Barnes, *Physical Review A* **99**, 052321 (2019).
- [32] E. Barnes, F. A. Calderon-Vargas, W. Dong, B. Li, J. Zeng, and F. Zhuang, *Quantum Science and Technology* **7**, 023001 (2022).
- [33] R. Carballera, D. Dolgitz, P. Zhao, D. Zeng, and Y. Chen, *Scientific Reports* **11**, 1 (2021).
- [34] A. Clerk, *SciPost Physics Lecture Notes*, 044 (2022).
- [35] X.-H. Deng, Y.-J. Hai, J.-N. Li, and Y. Song, *arXiv preprint arXiv:2103.08169* (2021).
- [36] S. Krunner, S. Lazar, A. Remm, C. Andersen, N. Lacroix, G. Norris, C. Hellings, M. Gabureac, C. Eichler, and A. Wallraff, *Physical Review Applied* **14**, 024042 (2020).
- [37] J. J. Burnett, A. Bengtsson, M. Scigliuzzo, D. Niepce, M. Kudra, P. Delsing, and J. Bylander, *npj Quantum Information* **5**, 1 (2019).
- [38] J. Lisenfeld, A. Bilmes, A. Megrant, R. Barends, J. Kelly, P. Klimov, G. Weiss, J. M. Martinis, and A. V. Ustinov, *npj Quantum Information* **5**, 1 (2019).
- [39] B. O'Neill, *Elementary differential geometry* (Elsevier, 2006).

- [40] A. N. Pressley, *Elementary differential geometry* (Springer Science & Business Media, 2010).
- [41] S. Blanes, F. Casas, J.-A. Oteo, and J. Ros, *Physics reports* **470**, 151 (2009).
- [42] L. H. Pedersen, N. M. Møller, and K. Mølmer, *Physics Letters A* **367**, 47 (2007).
- [43] P. Shor, “37th symposium on foundations of computing,” (1996).
- [44] A. Noiri, K. Takeda, T. Nakajima, T. Kobayashi, A. Sammak, G. Scappucci, and S. Tarucha, *Nature* **601**, 338 (2022).
- [45] M. T. Mađzik, S. Asaad, A. Youssry, B. Joecker, K. M. Rudinger, E. Nielsen, K. C. Young, T. J. Proctor, A. D. Baczewski, A. Laucht, *et al.*, *Nature* **601**, 348 (2022).
- [46] S. G. Philips, M. T. Mađzik, S. V. Amitonov, S. L. de Snoo, M. Russ, N. Kalhor, C. Volk, W. I. Lawrie, D. Brousse, L. Tryputen, *et al.*, *arXiv preprint arXiv:2202.09252* (2022).
- [47] W. Huang, C. Yang, K. Chan, T. Tanttu, B. Hensen, R. Leon, M. Fogarty, J. Hwang, F. Hudson, K. M. Itoh, *et al.*, *Nature* **569**, 532 (2019).
- [48] B. Bertrand, H. Flentje, S. Takada, M. Yamamoto, S. Tarucha, A. Ludwig, A. D. Wieck, C. Bäuerle, and T. Meunier, *Physical review letters* **115**, 096801 (2015).
- [49] M. Russ, D. M. Zajac, A. J. Sigillito, F. Borjans, J. M. Taylor, J. R. Petta, and G. Burkard, *Physical Review B* **97**, 085421 (2018).
- [50] A. Blais, A. L. Grimsmo, S. M. Girvin, and A. Wallraff, *Reviews of Modern Physics* **93**, 025005 (2021).
- [51] P. Krantz, M. Kjaergaard, F. Yan, T. P. Orlando, S. Gustavsson, and W. D. Oliver, *Applied Physics Reviews* **6**, 021318 (2019).
- [52] F. Motzoi, J. M. Gambetta, P. Rebentrost, and F. K. Wilhelm, *Physical review letters* **103**, 110501 (2009).
- [53] P. Zhao, K. Linghu, Z. Li, P. Xu, R. Wang, G. Xue, Y. Jin, and H. Yu, *PRX Quantum* **3**, 020301 (2022).
- [54] K. Wei, E. Magesan, I. Lauer, S. Srinivasan, D. Bogorin, S. Carnevale, G. Keefe, Y. Kim, D. Klaus, W. Landers, *et al.*, *arXiv preprint arXiv:2106.00675* (2021).
- [55] A. Kandala, K. Wei, S. Srinivasan, E. Magesan, S. Carnevale, G. Keefe, D. Klaus, O. Dial, and D. McKay, *Physical Review Letters* **127**, 130501 (2021).
- [56] P. Mundada, G. Zhang, T. Hazard, and A. Houck, *Physical Review Applied* **12**, 054023 (2019).
- [57] J. Ku, X. Xu, M. Brink, D. C. McKay, J. B. Hertzberg, M. H. Ansari, and B. Plourde, *Physical review letters* **125**, 200504 (2020).
- [58] Y. Xu, J. Chu, J. Yuan, J. Qiu, Y. Zhou, L. Zhang, X. Tan, Y. Yu, S. Liu, J. Li, *et al.*, *Physical Review Letters* **125**, 240503 (2020).
- [59] J. Stehlik, D. Zajac, D. Underwood, T. Phung, J. Blair, S. Carnevale, D. Klaus, G. Keefe, A. Carniol, M. Kumph, *et al.*, *Physical Review Letters* **127**, 080505 (2021).
- [60] Y. Sung, L. Ding, J. Braumüller, A. Vepsäläinen, B. Kannan, M. Kjaergaard, A. Greene, G. O. Samach, C. McNally, D. Kim, *et al.*, *Physical Review X* **11**, 021058 (2021).
- [61] F. Dyson *et al.*, *Nature* **427**, 297 (2004).
- [62] J. Mayer, K. Khairy, and J. Howard, *American Journal of Physics* **78**, 648 (2010).
- [63] A. A. Shabana, *ASME Open Journal of Engineering* **1** (2022).